

## MATERIALS SCIENCE

## Room temperature solid-state quantum emitters in the telecom range

Yu Zhou,<sup>1</sup> Ziyu Wang,<sup>1</sup> Abdullah Rasmita,<sup>1</sup> Sejeong Kim,<sup>2</sup> Amanuel Berhane,<sup>2</sup> Zoltán Bodrog,<sup>3</sup> Giorgio Adamo,<sup>1,4</sup> Adam Gali,<sup>3,5</sup> Igor Aharonovich,<sup>2\*</sup> Wei-bo Gao<sup>1,4\*</sup>

On-demand, single-photon emitters (SPEs) play a key role across a broad range of quantum technologies. In quantum networks and quantum key distribution protocols, where photons are used as flying qubits, telecom wavelength operation is preferred because of the reduced fiber loss. However, despite the tremendous efforts to develop various triggered SPE platforms, a robust source of triggered SPEs operating at room temperature and the telecom wavelength is still missing. We report a triggered, optically stable, room temperature solid-state SPE operating at telecom wavelengths. The emitters exhibit high photon purity (~5% multiphoton events) and a record-high brightness of ~1.5 MHz. The emission is attributed to localized defects in a gallium nitride (GaN) crystal. The high-performance SPEs embedded in a technologically mature semiconductor are promising for on-chip quantum simulators and practical quantum communication technologies.

## INTRODUCTION

In the last decade, SPEs have been explored as key resources for many quantum technologies (1–7), including quantum computation (8), quantum simulation (9–11), quantum metrology (12), and quantum communications (13–15), where the photons are used as “flying qubits”. In linear optical quantum computation, the information is carried by single photons that interact with each other through optical elements and projective measurements (8). In a Boson sampling quantum machine, single photons are used as inputs for a series of interferometers to complete photonic circuits (16). Furthermore, for most of the quantum key distribution (QKD) systems, single photons are the most fundamental building blocks (15). However, because of the lack of a practical ultrabright triggered SPE, current QKD systems widely use weak coherent pulse (from attenuated lasers). In this regard, a true SPE would still be preferred to achieve a longer secure distance and, thus, better performance.

For the above-mentioned applications, the operation wavelength is preferred to be in the telecom range because of its lower attenuation loss in fiber transmission performance as compared to shorter wavelengths. Current solutions for triggered SPEs at this wavelength range mostly rely on a variety of semiconductor quantum dots (QDs). For instance, InAs/InP QDs have single-photon emission at telecom wavelength (17) and have been used to realize 120-km QKD (18), whereas InAs/InGaAs QDs have been used for the generation of entangled photon pairs (19). However, these sources require cryogenic cooling down to liquid helium temperatures, which is not ideal for many scalable and practical devices. In a complementary approach, down-conversion of near-infrared photons to the telecom range was used (20). However, the photon generation is limited by the nonideal conversion efficiency in the nonlinear process. Finally, recent studies of chemically modified

single-walled carbon nanotubes showed optically stable, room temperature (RT) SPEs in the infrared spectral range (1.2 to 1.5  $\mu\text{m}$ ) (21).

Here, we report on unprecedented photostable, RT SPEs embedded in a GaN crystal and operating at the telecom range. The SPEs exhibit both excellent purity, with  $g^2(0) \sim 0.05$ , and a high brightness exceeding  $10^6$  counts/s. A number of GaN defects ranging from the ultraviolet (UV) to infrared wavelength have been predicted with a density functional study (22). However, most of the experimental studies have been focused on defects in the UV (23) and the visible range (24), whereas emitters in the infrared range remained largely unexplored. Moreover, because nanofabrication procedures with GaN are well established, the discovery of telecom SPEs can be instantly adopted and is highly promising for practical quantum technologies.

## RESULTS

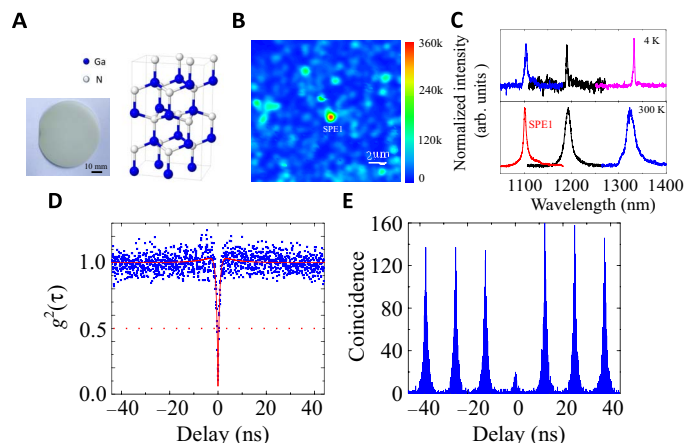
Figure 1A shows the GaN crystal structure and an optical image of a typical GaN wafer where SPEs were observed. The studied sample is a 2- $\mu\text{m}$ -thick magnesium (Mg)-doped GaN layer on a 2- $\mu\text{m}$  undoped GaN layer grown on sapphire. We first studied the photoluminescence (PL) spectra of GaN emitters with a home-built confocal scanning setup, where a 950-nm diode laser was used to excite the defect and emission above 1000 nm was collected and guided to a spectrometer or a pair of superconducting detectors in a Hanbury Brown-Twiss (HBT) configuration for photon counting (see Materials and Methods). Emitters are randomly distributed on the GaN substrate, and the confocal PL map around one of the SPEs, named as SPE1, is shown in Fig. 1B as an example. This particular defect emits ~350 kcounts/s at RT. A survey of the sample shows different SPEs with distinct narrowband emission, with zero phonon lines (ZPLs) ranging from 1085 to 1340 nm. The distribution of ZPLs will be discussed below. Examples of three SPEs at RT are given at the lower panel of Fig. 1C, whereas the top panel shows examples of three PL spectra of the SPEs recorded at cryogenic temperature (4 K). At RT, the full width at half maximum (FWHM) of the emitters' linewidth ranges from 3 nm (ZPL at 1120 nm) to 50 nm (ZPL at 1285 nm) (see fig. S1 for more information). At 4 K, the FWHM of the measured SPEs reduces to a few nanometers but is still broadened because of the coupling to the lattice phonons.

To confirm the nonclassical photon statistics from the studied emitters, we recorded the second-order autocorrelation function  $g^{(2)}(\tau)$ .

Copyright © 2018  
The Authors, some  
rights reserved;  
exclusive licensee  
American Association  
for the Advancement  
of Science. No claim to  
original U.S. Government  
Works. Distributed  
under a Creative  
Commons Attribution  
NonCommercial  
License 4.0 (CC BY-NC).

<sup>1</sup>Division of Physics and Applied Physics, School of Physical and Mathematical Sciences, Nanyang Technological University, Singapore 637371, Singapore. <sup>2</sup>Institute of Biomedical Materials and Devices, Faculty of Science, University of Technology Sydney, Ultimo, New South Wales 2007, Australia. <sup>3</sup>Wigner Research Centre for Physics, Institute for Solid State Physics and Optics, Hungarian Academy of Sciences, P.O. Box 49, H-1525 Budapest, Hungary. <sup>4</sup>The Photonics Institute and Centre for Disruptive Photonic Technologies, Nanyang Technological University, Singapore 637371, Singapore. <sup>5</sup>Department of Atomic Physics, Budapest University of Technology and Economics, Budafokúti 8, H-1111 Budapest, Hungary.

\*Corresponding author. Email: igor.aharonovich@uts.edu.au (I.A.); wbgao@ntu.edu.sg (W.-b.G.)



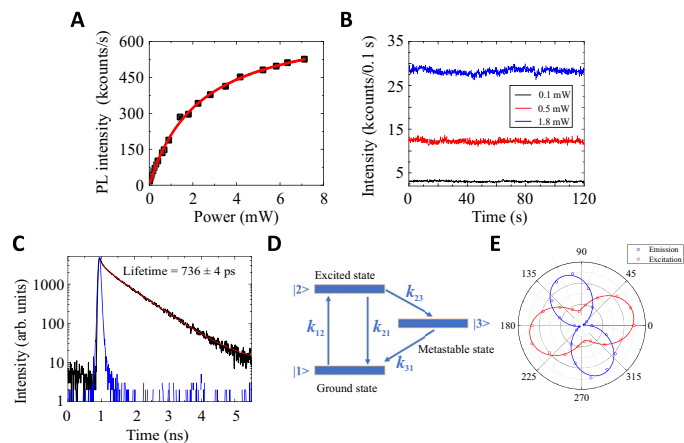
**Fig. 1. Infrared single-photon emission in GaN.** (A) Schematic illustration of GaN crystal structure and an optical image of the GaN wafer. (B) Confocal PL mapping with a single emitter SPE1 in the center of the map. (C) PL spectra of six infrared emitters, revealing that the PL ranges from 1085 to 1340 nm. PL spectra from three emitters are taken at 4 K (top) and 300 K (bottom), respectively. Note that the emitters at 4 K and RT are different. (D) Second-order correlation measurement of the emission from SPE1 under 950-nm cw laser excitation. The blue dots are the raw data without any background correction, and the red curve is the fitting to a three-level system, yielding  $g^2(0) = 0.05 \pm 0.02$ . (E) Second-order correlation measurement of SPE1 excited by pulsed laser with a 1-ps pulse width and a 80-MHz repetition rate, yielding  $g^2(0) = 0.14 \pm 0.01$ . The  $g^2(\tau)$  measurements were recorded at RT. arb. units, arbitrary units.

Figure 1D shows the  $g^{(2)}(\tau)$  recorded from SPE1 under continuous-wave (cw) laser excitation at RT. The peak at zero delay time indicates that the emission is nonclassical and the source is an SPE. Other emitters have similar properties, and more data can be found in the Supplementary Materials. The data are fit with a three-level model (Eq. 1)

$$g^2(\tau) = 1 - \alpha * \exp(-|\tau|/\tau_1) + \beta * \exp(-|\tau|/\tau_2) \quad (1)$$

where  $\tau_1$  and  $\tau_2$  are the excited state and the metastable state lifetimes, respectively, and  $\alpha$  and  $\beta$  are the fitting parameters. The obtained value at zero time delay  $g^2(0)$  is  $0.05 \pm 0.02$  without any background correction, proving that this is one of the purest RT SPEs. The slight deviation from zero is attributed to the background from other defects within the GaN crystal. Furthermore, as shown by the pulsed  $g^{(2)}(\tau)$  in Fig. 1E, the SPE can be efficiently triggered. To obtain the  $g^{(2)}(\tau)$  in a pulsed regime, we used pulsed laser excitation with a 80-MHz repetition rate and a 1-ps pulse width. The obtained value at zero delay time corresponds to  $g^2(0) = 0.14 \pm 0.01$ . It is also well below the classical threshold 0.5 for proving SPE. The value of  $g^2(0)$  under pulsed excitation is lifted because of the higher background in the pulse regime.

To study the performance of the SPEs in more details, we recorded a saturation curve from the emitter labeled SPE1 in Fig. 1B. More data are provided in the Supplementary Materials. Figure 2A shows the saturation behavior of SPE1 under cw laser excitation. The data are fit using the three-level system with an equation  $I_{(P)} = I_{\infty} \times P/(P + P_s)$ , where  $I_{(P)}$  is the measured intensity count rate,  $P$  is the excitation power, and  $P_s$  (saturation power) and  $I_{\infty}$  (maximum count) are two fitting parameters. For this particular emitter, we obtain  $P_s = 2.32 \pm 0.08$  mW and  $I_{\infty} = 0.69 \pm 0.01 \times 10^6$  counts/s. Such a count rate is on par with the brightest RT SPEs from a bulk crystal. The detailed discussion of extraction efficiency analysis is given in Materials and Methods.



**Fig. 2. Optical properties of SPE1.** (A) Saturation curve of SPE1 yielding a saturation power  $P_s = 2.32$  mW and  $I_{\infty} = 0.69$  Mcounts/s. (B) Photon stability measurement at three different excitation powers of 0.1 mW (black curve), 0.8 mW (red curve), and 1.5 mW (blue curve), respectively, over a period of 2 min. The time resolution is 100 ms, and no obvious blinking has been observed. (C) Fluorescence lifetime measurement of SPE1 (black curve) fit with a single exponent (red curve) yielding a lifetime  $\tau_1 = 736 \pm 4$  ps. The blue curve is the instrument response of the superconducting detector. (D) Schematic diagram of a three-level system used to describe the emitter. Detailed analysis of the transition rate can be found in the Supplementary Materials. (E) Polarization measurement of excitation (red open circle) and emission (blue open circle). The solid lines are the fitting with  $\cos^2(\theta)$ .

The source photostability is measured under low- and near-saturation excitation powers. The data are shown in Fig. 2B over an excitation period of 120 s under excitation powers of 0.1 mW (black curve), 0.5 mW (red curve), and 1.8 mW (blue curve). The time binning in this measurement is 100 ms, and no obvious blinking or bleaching was observed, proving the stability of the SPE. The fluorescence lifetime of the emitter is presented in Fig. 2C. The measured lifetime is  $736 \pm 4$  ps (black curve), which is in accordance with the value obtained from the  $g^{(2)}(\tau)$  fitting ( $776 \pm 39$  ps). The data were fit with single exponential function, and the instrument response function (blue curve) for our setup is shown for comparison in Fig. 2C. The system behaves according to a three-level model (Fig. 2D) with slight bunching at longer time scales (see the Supplementary Materials for the detailed rate equations). The polarization measurement of the emission and excitation is shown in Fig. 2E, fitting with  $\cos^2(\theta)$ . The polarization visibility  $\eta = (I_{\max} - I_{\min})/(I_{\max} + I_{\min})$  of emission and excitation is calculated to be 93.2 and 55.4%, respectively, which shows that it is a single linearly polarized dipole transition. Note that the emission orientation does not necessarily align with the crystallographic axis of GaN. The histogram of the emission dipole orientation of additional emitters is shown in fig. S2. Likewise, the angle between the absorption and emission dipoles varies from emitter to emitter (fig. S2).

To further optimize the brightness of the SPE by means of improving the photon extraction efficiency, we take advantage of the rather mature fabrication techniques of GaN. Rather than using top-down reactive ion etching techniques, a separate GaN sample is grown on a patterned sapphire substrate (PSS). The scanning electron microscopy image of such a structure is shown in Fig. 3A. This structure is designed and extensively used for the light-emitting diode emission enhancement by increasing the reflection area and therefore improving the light extraction efficiency.

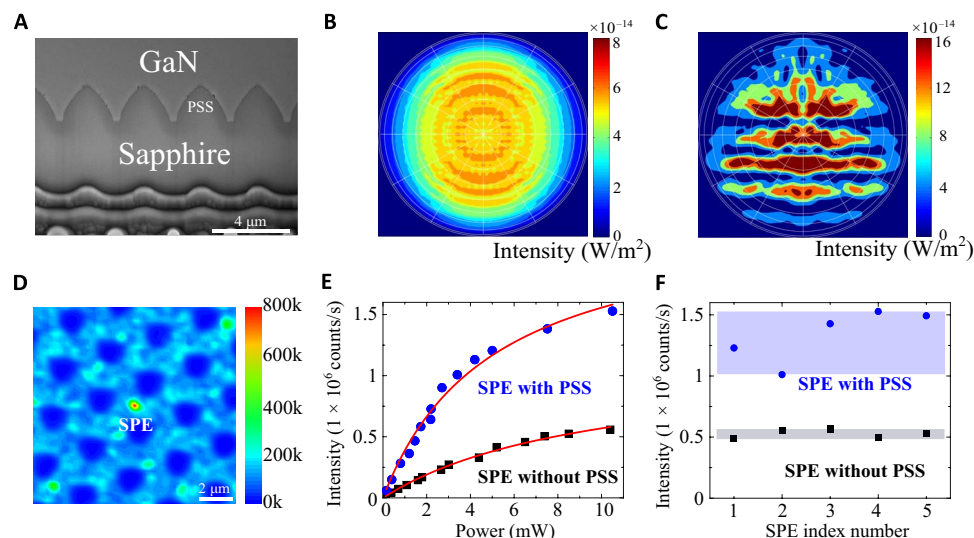


**Fig. 3. Enhancement of SPEs in GaN using a PSS.** (A) SEM image of the cross section of the GaN grown on a PSS. Cone shapes of the PSS are seen. (B) Far-field radiation pattern of the in-plane dipole in the pristine GaN wafer. The circles represent collection half-angles from 100 to 900 (inner to outer circles). (C) Far-field radiation pattern of the in-plane dipole in the GaN grown on top of a PSS. Note that the maximum intensity in (C) is two times higher than that in (B). (D) Confocal scan map of an SPE in GaN grown on PSS, with the blue circles corresponding to the PSS cones. (E) Saturation curves comparing between an SPE in a pristine GaN (black squares) with an SPE embedded in a GaN grown on a PSS (blue circles). The saturated emission ( $I_{\infty}$ ) for SPE with PSS reaches  $2.33 \times 10^6$  counts/s compared to only  $1.13 \times 10^6$  counts/s from pristine GaN. The red curve is the fitting function of the raw data. (F) Comparison of count rate at 10 mW for five emitters from pristine GaN (black squares) and five emitters from GaN grown on the PSS (blue circles). The shaded rectangles serve as visual guides. The full saturation curves are presented in the Supplementary Materials.

To study the effect of the PSS on the extraction efficiency, we carried out three-dimensional (3D) finite difference time domain (FDTD) optical simulation (using Lumerical software) for the defect embedded in a pristine GaN and the one grown on a PSS. On the basis of the simulation results, the far-field pattern and the collection efficiency can be obtained (25). For the bare GaN substrate, a model consisting of a GaN layer (refractive index, 2.33) on top of a sapphire layer (refractive index, 1.75) in an immersion oil environment (refractive index, 1.52) is assumed. For the GaN/PSS structure, the model is modified to include the patterned geometry (see fig. S3 for the illustration). The FDTD simulation provides the far-field radiation patterns for the emitter in a pristine GaN and in a GaN/PSS structure, as seen in Fig. 3 (B and C, respectively). Note that the maximum intensity in Fig. 3C is higher than that in Fig. 3B. The power collected within 620 half-angle [that is, the maximum collected half-angle for a 1.35-numerical aperture (NA) objective in an immersion oil environment] of the far-field radiation is then calculated for both cases. By comparing these calculation results, it is found that an enhancement up to approximately two times is expected when the PSS is used. This enhancement is attributed to the additional light focusing provided by the V-shaped region between two cones of the PSS.

Upon scanning the sample, similar SPEs emitters with the one shown in Fig. 1 can be easily detected. This is evident from the confocal map in Fig. 3D. The blue pattern corresponds to the PSS structure underneath the surface. Figure 3E shows a saturation curve for an SPE on a pristine GaN sample compared to that embedded in the GaN grown on PSS. The increase in count rate is observed. The SPEs located in the center of the PSS pattern exhibits an enhanced count rate reaching  $2.33 \times 10^6$  counts/s at saturation compared to a saturation rate of  $1.13 \times 10^6$  counts/s for another SPE in a pristine GaN. The counts for samples on PSS correspond to an enhancement factor of  $\sim 2$  as compared with the ones without PSS, consistent with the Lumerical simula-

tions. Figure 3F shows a statistical count comparison of 10 different emitters that convincingly proves the overall enhancement (details shown in figs. S4 to S8).

Finally, we discuss the possible origin of our emitters. The experimental data imply that most of the observed SPEs should have a common origin, but the environment is diverse around these emitters. On the basis of the materials characterization, it is unlikely that strain may induce such a wide wavelength distribution. We rather consider the model of an optically active point defect near cubic inclusions within the hexagonal lattice of GaN (24). The PL energies are calculated with a simple quasi-1D model, where a point defect resides in the proximity of the cubic inclusion. The luminescence is the result of an exciton recombination, where the hole is tightly localized at the point defect, whereas the loosely localized electron's position is more influenced by the potential lineup generated by the stacking sequence of cubic and hexagonal GaN bilayers. Thus, the binding energy of the exciton and PL wavelength are determined by the relative position of the point defect with respect to the cubic inclusion. Figure 4 (A and B) shows the distribution of the ZPLs obtained for a single- and double-cubic inclusion that result in a broad distribution of the ZPLs. The configuration of multiple cubic inclusions fits the presented experimental data well. If the defect is located exactly at the interface of the cubic/hexagonal boundary, then PL lines are expected to occur only at the lower ( $\sim 1100$  nm) and the higher ( $\sim 1350$  nm) wavelength range. Both emission wavelengths were experimentally observed in our experiments (see Fig. 4C). Note that the emission SPE at  $1.55 \mu\text{m}$  is also possible with our model. Figure S9 shows the span of ZPL wavelengths when the point defect in a perfect h-GaN emits at  $\sim 1450$  nm nearby a cubic inclusion. The emission ensemble at these wavelengths was observed previously in GaN (26, 27).

Although the presented model explains well the ZPL shifts observed in our work, the origin of the luminescent impurity remains unknown,

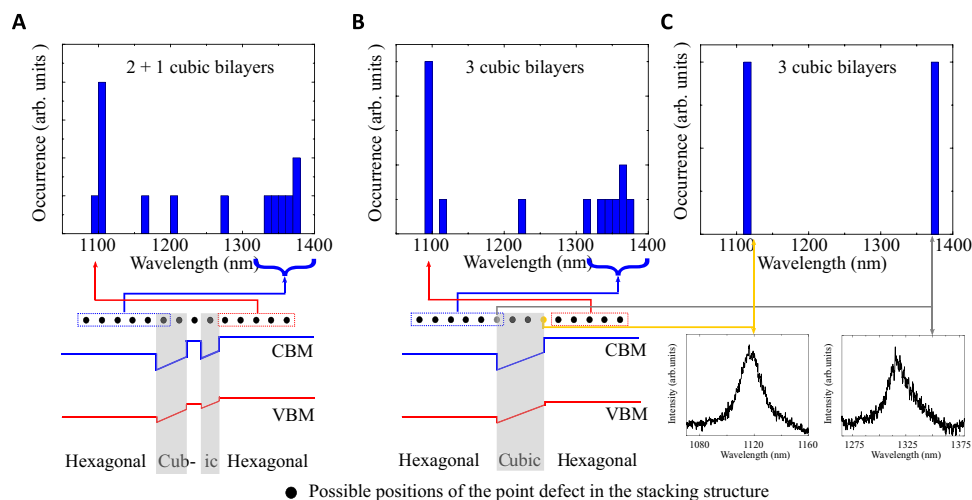


**Fig. 4. Numerical modeling of the SPEs.** (A and B) Theoretical spectral distribution resulting from point defects distributed between cubic inclusions in a 2 + 1 bilayer configuration and a continuous 3 cubic bilayer configuration, respectively. The blue columns correspond to the spectral position of the emitters' ZPL. The arrows connect possible positions of the point defect (distributed uniformly in each GaN bilayer in the neighborhood of the cubic inclusion) and the resulting spectral positions of the ZPL. (C) If the point defects are located solely at the interface, then only two distinctive ZPLs are visible at ~1100 and 1350 nm. Our experimental data matches well with the scenario in (A) and a particular configuration in (C). Two spectra are shown to exemplify the match between the predicted and the observed PL. CBM and VBM denote the conduction band minimum and valence band maximum, respectively, and five emitters from GaN grown on the PSS (blue circles). The shaded rectangles serve as visual guides. The full saturation curves are presented in the Supplementary Materials.

and probably not all the emitters are of exactly the same type. So far, there is no evidence in the literature on a RT narrowband emission (even from ensembles) from GaN in the infrared spectral range. Luminescence at ~1.5  $\mu\text{m}$  was reported from GaN wafers implanted with Er ions (the emission is an internal transition of Er) (28), whereas the broad PL (only at cryogenic temperatures) from high-energy electron irradiation and annealing was reported at ~0.9 eV and was attributed tentatively to Ga interstitials (27). Other works observed narrowband luminescence around ~1 eV (also at cryogenic temperature) that was attributed to Cr impurities (29, 30). Further density functional theory (DFT) calculations and targeted ion implantation experiments into ultrapure GaN crystals will be required before the absolute crystallographic structure of the quantum emitters can be unveiled.

## DISCUSSION

Overall, we reported on ultrabright, optically stable, single-photon emission in GaN at the telecom range. The SPEs operate at RT and have FWHM as small as ~3 nm. Furthermore, we demonstrated that these emitters can be observed in commercially available, pristine GaN wafers without the necessity of electron or ion irradiation, and their emission rates can reach megahertz rates upon substrate patterning. Several immediate research directions come out of our work. First, unveiling the origin of the emitters via DFT modeling in conjunction with ion implantation and growth should be feasible and within reach. Above-bandgap excitation of these emitters should be investigated to understand the underlying excitation pathways. In addition, doping techniques of GaN are well developed, and optoelectronic components with p-i-n layers are available (31). It may therefore be possible to realize electrically triggered RT SPE in the telecom range—a highly crucial component for scalable devices (31, 32). Furthermore, photonic cavities and waveguides can be engineered relatively easy from GaN (33, 34), paving the way to an on-chip integrated quantum nanophotonics platform

(4, 35–38). Finally, investigating the spin properties of these defects can become useful to explore spin-photon interfaces (6) in GaN for quantum information processing.

## MATERIALS AND METHODS

### Experimental setup

For the RT measurement, the samples were mounted on a 3D nanopositioner (PI P-611.3S) for confocal PL map scanning. A diode laser with a wavelength of 950 nm was used for cw excitation, and a titanium/sapphire 1-ps laser with a 80-MHz repetition rate (Spectra-Physics) was used for pulse excitation. The laser beam passed through a 1000-nm short-pass filter to clean up the residual spectrum above 1000 nm and was then focused down with an oil objective with a NA of 1.35 (Nikon). The collected light went through the same objective into a single-mode fiber that was used as a confocal aperture. The signal was then guided to low-jitter (~30 ps) superconducting single-photon detectors (SSPDs; Scotel) for counting or a liquid nitrogen-cooled InGaAs camera (Princeton Instruments) for spectrum analysis. For the HBT interferometer setup, the PL signal was divided with a fiber beam splitter and detected by two SSPDs. The correlation coincidence was recorded by a time-correlated photon-counting card (PH300, PicoHarp). For the cryogenic measurements, the sample was mounted in a closed-cycle cryostat (Montana Instruments) equipped with at-cube steppers for the rough scanning and galvo mirrors above the cryostat for the fine scanning.

### Sample description

For the data in Figs. 1 and 2, we used GaN with a 2- $\mu\text{m}$ -thick Mg-doped GaN layer on a 2- $\mu\text{m}$  undoped GaN layer grown on planar sapphire. For the data in Fig. 3, 6.5- $\mu\text{m}$  GaN was grown on a PSS with cone structures. The cone patterns had a width of 2.5  $\mu\text{m}$  and a height of 1.7  $\mu\text{m}$ , with a separation distance of 3  $\mu\text{m}$ .

## SUPPLEMENTARY MATERIALS

Supplementary material for this article is available at <http://advances.sciencemag.org/cgi/content/full/4/3/eaar3580/DC1>

section S1. PL statistics and PL under high powers

section S2. Polarization statistics

section S3. Second-order correlation fitting procedure

section S4. Model to compare SPEs with and without PSS

section S5. Comparison between SPEs in pristine GaN and SPEs in GaN grown on PSS

section S6. Modeling of a proposed defect structure

fig. S1. PL statistics of GaN emitters and PL under high power.

fig. S2. Polarization statistics of GaN emitters.

fig. S3. Photon antibunching measurement of SPE1.

fig. S4. Model of SPE in GaN with PSS structure.

fig. S5. PLs and saturation curves of SPEs in pristine GaN.

fig. S6. Second-order autocorrelation function of five SPEs in pristine GaN.

fig. S7. PLs and saturation curves of SPEs grown on PSS.

fig. S8. Second-order autocorrelation function of five SPEs in GaN grown on PSS.

fig. S9. Span of ZPL wavelengths when the point defect in perfect h-GaN emits at 1450 nm nearby a cubic inclusion.

table S1. Summary of measured lifetimes and maximum counts of SPE A to E in pristine GaN and SPE a to e in GaN grown on PSS.

References (39–41)

## REFERENCES AND NOTES

- I. Aharonovich, D. Englund, M. Toth, Solid-state single-photon emitters. *Nat. Photonics* **10**, 631–641 (2016).
- J. L. O'Brien, A. Furusawa, J. Vučković, Photonic quantum technologies. *Nat. Photonics* **3**, 687–695 (2009).
- A. Sipahigil, R. E. Evans, D. D. Sukachev, M. J. Burek, J. Borregaard, M. K. Bhaskar, C. T. Nguyen, J. L. Pacheco, H. A. Atikian, C. Meuwly, R. M. Camacho, F. Jelezko, E. Bielejec, H. Park, M. Lončar, M. D. Lukin, An integrated diamond nanophotonics platform for quantum optical networks. *Science* **354**, 847–850 (2016).
- P. Lodahl, S. Mahmoodian, S. Stobbe, Interfacing single photons and single quantum dots with photonic nanostructures. *Rev. Mod. Phys.* **87**, 347–400 (2015).
- K. Müller, A. Rundquist, K. A. Fischer, T. Sarmiento, K. G. Lagoudakis, Y. A. Kelaita, C. Sánchez Muñoz, E. del Valle, F. P. Laussy, J. Vučković, Coherent generation of nonclassical light on chip via detuned photon blockade. *Phys. Rev. Lett.* **114**, 233601 (2015).
- W. B. Gao, A. Imamoglu, H. Bernien, R. Hanson, Coherent manipulation, measurement and entanglement of individual solid-state spins using optical fields. *Nat. Photonics* **9**, 363–373 (2015).
- T. E. Northup, R. Blatt, Quantum information transfer using photons. *Nat. Photonics* **8**, 356–363 (2014).
- P. Kok, W. J. Munro, K. Nemoto, T. C. Ralph, J. P. Dowling, G. J. Milburn, Linear optical quantum computing with photonic qubits. *Rev. Mod. Phys.* **79**, 135–174 (2007).
- I. M. Goguescu, S. Ashhab, F. Nori, Quantum simulation. *Rev. Mod. Phys.* **86**, 153–185 (2014).
- N. C. Harris, G. R. Steinbrecher, M. Prabhu, Y. Lahini, J. Mower, D. Bunandar, C. Chen, F. N. C. Wong, T. Baehr-Jones, M. Hochberg, S. Lloyd, D. Englund, Quantum transport simulations in a programmable nanophotonic processor. *Nat. Photonics* **11**, 447–452 (2017).
- A. Aspuru-Guzik, P. Walther, Photonic quantum simulators. *Nat. Phys.* **8**, 285–291 (2012).
- V. Giovannetti, S. Lloyd, L. Maccone, Quantum metrology. *Phys. Rev. Lett.* **96**, 010401 (2006).
- J. Nilsson, R. M. Stevenson, K. H. A. Chan, J. Skiba-Szymanska, M. Lucamarini, M. B. Ward, A. J. Bennett, C. L. Salter, I. Farrer, D. A. Ritchie, A. J. Shields, Quantum teleportation using a light-emitting diode. *Nat. Photonics* **7**, 311–315 (2013).
- J. Yin, Y. Cao, Y.-H. Li, S.-K. Liao, L. Zhang, J.-G. Ren, W.-Q. Cai, W.-Y. Liu, B. Li, H. Dai, G.-B. Li, Q.-M. Lu, Y.-H. Gong, Y. Xu, S.-L. Li, F.-Z. Li, Y.-Y. Yin, Z.-Q. Jiang, M. Li, J.-J. Jia, G. Ren, D. He, Y.-L. Zhou, X.-X. Zhang, N. Wang, X. Chang, Z.-C. Zhu, N.-L. Liu, Y.-A. Chen, C.-Y. Lu, R. Shu, C.-Z. Peng, J.-Y. Wang, J.-W. Pan, Satellite-based entanglement distribution over 1200 kilometers. *Science* **356**, 1140–1144 (2017).
- H.-K. Lo, M. Curry, K. Tamaki, Secure quantum key distribution. *Nat. Photonics* **8**, 595–604 (2014).
- H. Wang, Y. He, Y.-H. Li, Z.-E. Su, B. Li, H.-L. Huang, X. Ding, M.-C. Chen, C. Liu, J. Qin, J.-P. Li, Y.-M. He, C. Schneider, M. Kamp, C.-Z. Peng, S. Höfling, C.-Y. Lu, J.-W. Pan, High-efficiency multiphoton boson sampling. *Nat. Photonics* **11**, 361–365 (2017).
- J.-H. Kim, T. Cai, C. J. K. Richardson, R. P. Leavitt, E. Waks, Two-photon interference from a bright single-photon source at telecom wavelengths. *Optica* **3**, 577–584 (2016).
- K. Takemoto, Y. Nambu, T. Miyazawa, Y. Sakuma, T. Yamamoto, S. Yoroazu, Y. Arakawa, Quantum key distribution over 120 km using ultrahigh purity single-photon source and superconducting single-photon detectors. *Sci. Rep.* **5**, 14383 (2015).
- M. B. Ward, M. C. Dean, R. M. Stevenson, A. J. Bennett, D. J. P. Ellis, K. Cooper, I. Farrer, C. A. Nicoll, D. A. Ritchie, A. J. Shields, Coherent dynamics of a telecom-wavelength entangled photon source. *Nat. Commun.* **5**, 3316 (2014).
- K. De Greve, L. Yu, P. L. McMahon, J. S. Pelc, C. M. Natarajan, N. Y. Kim, E. Abe, S. Maier, C. Schneider, M. Kamp, S. Höfling, R. H. Hadfield, A. Forchel, M. M. Fejer, Y. Yamamoto, Quantum-dot spin-photon entanglement via frequency downconversion to telecom wavelength. *Nature* **491**, 421–425 (2012).
- X. He, N. F. Hartmann, X. Ma, Y. Kim, R. Ihly, J. L. Blackburn, W. Gao, J. Kono, Y. Yomogida, A. Hirano, T. Tanaka, H. Kataura, H. Htoon, S. K. Doorn, Tunable room-temperature single-photon emission at telecom wavelengths from  $sp^3$  defects in carbon nanotubes. *Nat. Photonics* **11**, 577–582 (2017).
- A. Alkauskas, J. L. Lyons, D. Steiauf, C. G. Van de Walle, First-principles calculations of luminescence spectrum line shapes for defects in semiconductors: The example of GaN and ZnO. *Phys. Rev. Lett.* **109**, 267401 (2012).
- M. Arita, F. Le Roux, M. J. Holmes, S. Kako, Y. Arakawa, Ultraclean single photon emission from a GaN quantum dot. *Nano Lett.* **17**, 2902–2907 (2017).
- A. M. Berhane, K.-Y. Jeong, Z. Brodog, S. Fiedler, T. Schröder, N. V. Triviño, T. Palacios, A. Gali, M. Toth, D. Englund, I. Aharonovich, Bright room-temperature single-photon emission from defects in gallium nitride. *Adv. Mater.* **29**, 1605092 (2017).
- S. Kim, S.-H. Gong, J.-H. Cho, Y.-H. Cho, Unidirectional emission of a site-controlled single quantum dot from a pyramidal structure. *Nano Lett.* **16**, 6117–6123 (2016).
- I. Buyanova, M. Wagner, W. Chen, B. Monemar, J. Lindström, H. Amano, I. Akasaki, Photoluminescence of GaN: Effect of electron irradiation. *Appl. Phys. Lett.* **73**, 2968–2970 (1998).
- M. Linde, S. J. Uffring, G. D. Watkins, V. Härle, F. Scholz, Optical detection of magnetic resonance in electron-irradiated GaN. *Phys. Rev. B* **55**, R10177–R10180 (1997).
- M. Thaik, U. Hömmerich, R. N. Schwartz, R. G. Wilson, J. M. Zavada, Photoluminescence spectroscopy of erbium implanted gallium nitride. *Appl. Phys. Lett.* **71**, 2641–2643 (1997).
- K. Pressel, S. Nilsson, R. Heitz, A. Hoffmann, B. K. Meyer, Photoluminescence study of the 1.047 eV emission in GaN. *J. Appl. Phys.* **79**, 3214–3218 (1996).
- W. F. Koehl, B. Diler, S. J. Whiteley, A. Bourassa, N. T. Son, E. Janzén, D. D. Awschalom, Resonant optical spectroscopy and coherent control of  $Cr^{4+}$  spin ensembles in SiC and GaN. *Phys. Rev. B* **95**, 035207 (2017).
- S. Deshpande, J. Heo, A. Das, P. Bhattacharya, Electrically driven polarized single-photon emission from an InGaN quantum dot in a GaN nanowire. *Nat. Commun.* **4**, 1675 (2013).
- N. Mizuochi, T. Makino, H. Kato, D. Takeuchi, M. Ogura, H. Okushi, M. Nothhaft, P. Neumann, A. Gali, F. Jelezko, J. Wrachtrup, S. Yamasaki, Electrically driven single-photon source at room temperature in diamond. *Nat. Photonics* **6**, 299–303 (2012).
- N. V. Triviño, G. Rossbach, U. Dharanipathy, J. Levrat, A. Castiglia, J. F. Carlin, K. A. Atlasov, R. Butte, R. Houdre, N. Grandjean, High quality factor two dimensional GaN photonic crystal cavity membranes grown on silicon substrate. *Appl. Phys. Lett.* **100**, 071103 (2012).
- A. Woolf, T. Puchler, I. Aharonovich, T. Zhu, N. Niu, D. Wang, R. Oliver, E. L. Hu, Distinctive signature of indium gallium nitride quantum dot lasing in microdisk cavities. *Proc. Natl. Acad. Sci. U.S.A.* **111**, 14042–14046 (2014).
- J. Claudon, J. Bleuse, N. S. Malik, M. Bazin, P. Jaffrennou, N. Gregersen, C. Sauvan, P. Lalanne, J.-M. Gérard, A highly efficient single-photon source based on a quantum dot in a photonic nanowire. *Nat. Photonics* **4**, 174–177 (2010).
- N. Somaschi, V. Giesz, L. De Santis, J. Loredò, M. Almeida, G. Hornecker, S. Portalupi, T. Grange, C. Antón, J. Demory, C. Gómez, I. Sagnes, N. D. Lanzillotti-Kimura, A. Lemaître, A. Auffeves, A. G. White, L. Lanco, P. Senellart, Near-optimal single-photon sources in the solid state. *Nat. Photonics* **10**, 340–345 (2016).
- M. Pelton, Modified spontaneous emission in nanophotonic structures. *Nat. Photonics* **9**, 427–435 (2015).
- O. Benson, Assembly of hybrid photonic architectures from nanophotonic constituents. *Nature* **480**, 193–199 (2011).
- C. Kurtsiefer, S. Mayer, P. Zarda, H. Weinfurter, Stable solid-state source of single photons. *Phys. Rev. Lett.* **85**, 290–293 (2000).
- A. Belabbes, L. de Carvalho, A. Schleife, F. Bechstedt, Cubic inclusions in hexagonal AlN, GaN, and InN: Electronic states. *Phys. Rev. B* **84**, 125108 (2011).
- M. E. Levinstein, S. L. Rumyantsev, M. S. Shur, *Properties of Advanced Semiconductor Materials: GaN, AlN, InN, BN, SiC, SiGe* (John Wiley & Sons, 2001).

## Acknowledgments

**Funding:** We acknowledge the support from the Singapore National Research Foundation through a Singapore 2015 National Research Foundation fellowship grant (NRF-NRFF2015-03) and its Competitive Research Program (CRP award no. NRF-CRP14-2014-02), Singapore Ministry of Education (RG176/15, MOE2016-T2-2-077, and MOE2011-T3-1-005), A\*Star QTE program, and a start-up grant (M4081441) from Nanyang Technological University. I.A. acknowledges the Air Force Office of Scientific Research, U.S. Air Force (grant FA2386-17-1-4064), and the Office of Naval Research Global under grant number N62909-18-1-2025. A.G. acknowledges the support from the National Research Development and Innovation Office of Hungary within the Quantum Technology National Excellence Program (project no. 2017-1.2.1-NKP-2017-00001). **Author**

**contributions:** Y.Z. and Z.W. built the optical setup and performed the optical measurements. Y.Z., A.R., and S.K. performed the data analysis. Z.B. and A.G. performed the wavelength modeling. A.B. and G.A. assisted with sample preparation. Y.Z., I.A., and W.-b.G. designed the experiments and wrote the manuscript with contributions from all coauthors. All authors contributed to the discussion of the results. **Competing interests:** The authors declare that they have no competing interests. **Data and materials availability:** All data needed to evaluate the conclusions in the paper are present in the paper and/or the Supplementary Materials. Additional data related to this paper may be requested from the authors.

Submitted 30 October 2017

Accepted 13 February 2018

Published 30 March 2018

10.1126/sciadv.aar3580

**Citation:** Y. Zhou, Z. Wang, A. Rasmita, S. Kim, A. Berhane, Z. Bodrog, G. Adamo, A. Gali, I. Aharonovich, W.-b. Gao, Room temperature solid-state quantum emitters in the telecom range. *Sci. Adv.* **4**, eaar3580 (2018).